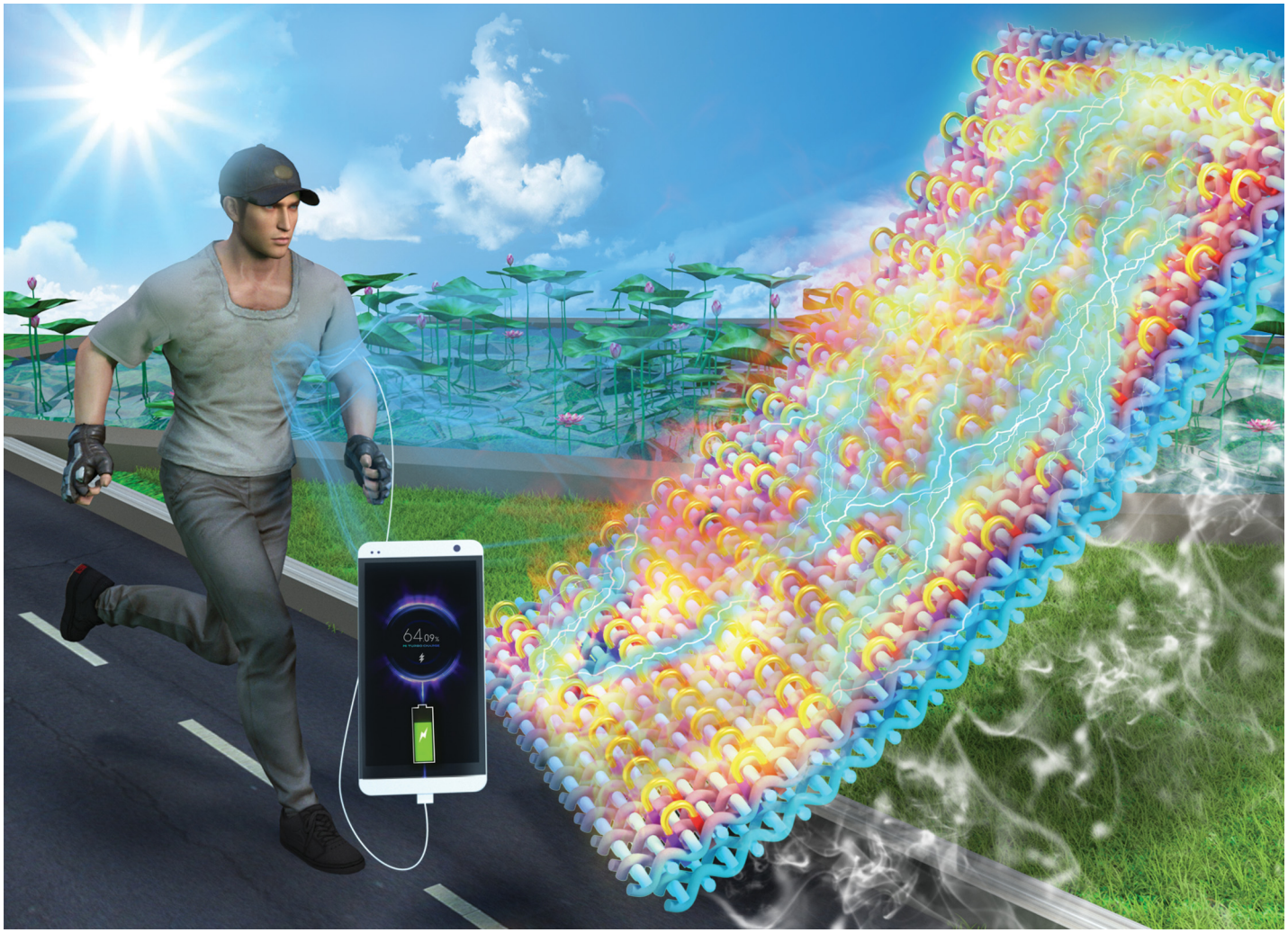

Showcasing research from Professor Kun Zhang's laboratory, College of Textiles, Donghua University, Shanghai, China.

Durable, stretchable and washable inorganic-based woven thermoelectric textiles for power generation and solid-state cooling

In this work, we design and produce Bi_2Te_3-based, hierarchically segmented ternary coaxial TE strings at large scale for semi-automatically manufacture of highly mechanically stable, stretchable and washable woven TETs by textile process. The TET can continuously power on-body electronics. Furthermore, the TET can stably generate solid-state cooling of 3.1 K in quiescent air.

As featured in:

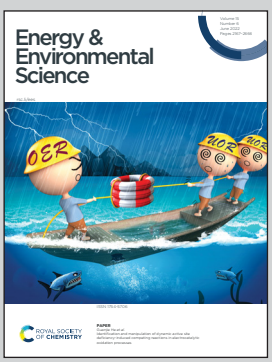

See Guodong Li, Kun Zhang *et al.*, *Energy Environ. Sci.*, 2022, **15**, 2374.

ROYAL SOCIETY OF CHEMISTRY

rsc.li/ees

Registered charity number: 207890

Energy & Environmental Science

ROYAL SOCIETY OF CHEMISTRY

PAPER

View Article Online
View Journal | View Issue

Cite this: *Energy Environ. Sci.*, 2022, **15**, 2374

Durable, stretchable and washable inorganic-based woven thermoelectric textiles for power generation and solid-state cooling†

Yuanyuan Zheng,[a] Xue Han,[a] Jiawei Yang,[bc] Yuanyuan Jing,[a] Xinyi Chen,[a] Qianqian Li,[ad] Ting Zhang,[ef] Guodong Li,*[b] Hangtian Zhu,[b] Huaizhou Zhao,[b] G. Jeffrey Snyder[g] and Kun Zhang*[a]

Wearable inorganic semiconductor (ISC) based thermoelectric (TE) devices, especially fiber-based thermoelectric textiles (TETs), show promise in electrical power generation and solid-state cooling compared with bulk ISC-based TE generators (TEGs). However, it is challenging to use the ISCs, with brittleness and mechanical instability, to produce thermoelectric fibers for weaving TETs. Here, we report a strategy to produce ISC-based segmented hierarchically ternary coaxial TE strings at large scale for semi-automatically manufacturing a highly mechanically stable, stretchable, breathable and washable woven TET by a textile machine. The TET demonstrates good stretchability (100% elongation), flexibility (bending radius of 2 mm), washability (>20 washing cycles) and output power density of 0.58 W m^{-2} at a temperature difference of 25 K (predicted power density of 6.06 W m^{-2} at ΔT = 80 K). With the assistance of finite element analysis, the significance of the fabric's structure on the excellent mechanical and TE performance of the TET has been clarified, which reaches an output voltage of ~0.28 V at an ambient temperature of ~8 °C. For practical applications, it can continuously power on-body electronics for monitoring the environment and the human body's vital signals and activities by wearing it on the arm with a self-built temperature gradient of ~16 K. Furthermore, the TET can stably generate solid-state cooling of 3.1 K in quiescent air ($T_{ambient}$ ~ 26 °C, relative humidity ~60%). This work paves a new way for designing durable, stretchable and washable ISC-based TETs toward real on-body applications.

Received 22nd November 2021,
Accepted 3rd March 2022

DOI: 10.1039/d1ee03633e

rsc.li/ees

Broader context

Wearable thermoelectric devices are promising to power portable electronics and realize personal thermoregulation. Compared with other types of wearable thermoelectric devices, such as flexible film based ones, thermoelectric textiles possess three-dimensional conformability to the dynamic curved surface of the human body, thermal comfortability and durability, which are indispensable in realistic wearing scenarios. However, it is still very challenging to design thermoelectric textiles with high output performance, excellent mechanical properties and washability. In this work, we design and produce machine-weavable Bi_2Te_3-based TE strings with enhanced mechanical and TE properties to fabricate a TET using a commercial semi-automatic weaving machine, which shows high power generation, notable solid-state cooling ability, excellent flexibility, stretchability and cycling stability, as well as washability. This work paves a new way to design truly wearable thermoelectric textiles.

[a] *Key Laboratory of Textile Science & Technology (Ministry of Education), College of Textiles, Donghua University, Shanghai, 201620, P. R. China. E-mail: kun.zhang@dhu.edu.cn*
[b] *Beijing National Laboratory for Condensed Matter Physics, Institute of Physics, Chinese Academy of Sciences, Beijing, 100190, P. R. China. E-mail: gdli@iphy.ac.cn*
[c] *School of Physical Sciences, University of Chinese Academy of Sciences, Beijing, 100049, P. R. China*
[d] *Shanghai Collaborative Innovation Center for High Performance Fiber Composites, Donghua University, Shanghai, 201620, P. R. China*
[e] *Institute of Engineering Thermophysics, Innovation Academy for Light-duty Gas Turbine, Chinese Academy of Sciences, Beijing, 100190, P. R. China*
[f] *Nanjing Institute of Future Energy System, Nanjing, 211135, P. R. China*
[g] *Department of Materials Science and Engineering, Northwestern University, Evanston, IL 60208, USA*

† Electronic supplementary information (ESI) available. See DOI: 10.1039/d1ee03633e

1. Introduction

For on-body applications, it is urgent to develop a durable and wearable power supply system for Internet of Things (IoT) electronics and personal thermoregulation. Compared with other kinds of power generation,[1–3] flexible thermoelectric generators (TEGs) can noiselessly and continuously convert heat into electricity.[4–6] On the other hand, they can also be used as solid-state cooling for personal thermoregulation. In contrast to traditional air conditioners, they are portable and refrigerant free.[7] In addition, compared with passive radiative

coolers,[8] they can stably decrease the temperature to sub-ambient and are not affected by ambient temperature and moisture, as well as dyeing processes *etc.*

However, the utmost challenge involves developing rational ways to facilely design and manufacture three-dimensional (3D) architectured TEGs at a large scale with good wearability, including dynamic surface conformability (twistability, bendability and stretchability), breathability, washability and thermo-comfortability, as well as high thermoelectric performances (power generation and solid-state cooling). Thermoelectric textiles (TETs) are promising for addressing the aforementioned challenge towards truly breathable daily-wear TE devices because they can be manufactured by using traditional textile yarns and TE yarns. However, it is still very challenging to fabricate large-scale TETs due to the lack of concurrency of excellent scalability, weavability and TE properties of p–n segmented TE yarns, which are ideally configured with p-type and n-type TE fiber segments alternately interconnected electrically in series and thermally in-parallel for industrial textile processes.

Recent organic-based TETs using segmented TE yarns are inherently wearable and can conform to the dynamic curved body surface.[9] However, they still suffer from relatively low power generation (*e.g.* $\sim 10^{-3}$–10^{0} nW cm^{-2} at a temperature difference (ΔT) of $\sim$20 K[9,10]). In realistic conditions, the foremost concern is to have either high ΔT (10^{1}–10^{2} kelvins[11]) or a large density of TE pillars[4] for sufficient power generation. However, the practical ΔT is typically 5–15 K in realistic scenarios and the pillar density is constrained by the fabric density during industrial textile process.

Hence, high-*ZT*-value inorganic semiconductors (ISCs, *e.g.* Bi_2Te_3-based TE materials), with a rigid and brittle nature, have been reconsidered to develop flexible TETs with high TE power generation and solid-state cooling.[12–16] For flexible TETs, it is of vital importance and more convenient to suppress rigidity by re-designing ISC based TETs in terms of the device configuration rather than by time-and-cost consuming material engineering.[17–19] Recently, two main strategies have been developed to realize flexibility. One is *via* thermally drawing ISCs into filaments[20,21] and the other one is by coating ISCs on yarns/fabrics.[10,22,23] During deformation, both ISCs and textile substrates absorb the mechanical energy. Nevertheless, ISCs tend to appear brittle fracture under deformation, resulting in its exfoliation from substrates, thus leading to the ultimate failure of the TETs.[24] Therefore, the toughness and mechanical stability of ISCs, which are strongly correlated with the ability of resisting crack propagation and improving energy absorption, must be essentially enhanced to obtain durable TETs. Generally, toughness and mechanical stability can be improved by adding a reinforcement phase, such as electrically insulating fibers and particles.[25] However, this will significantly deteriorate the *ZT* values of ISCs. Hence, big challenges still remain to obtain ISC based TETs with high thermoelectric power generation and solid-state cooling, as well as boosted toughness and mechanical stability.

Here, we develop a mechanically stable TE string configuration with alternating p-type $Bi_{0.4}Sb_{1.3}Te_3$ (BST) and n-type $Bi_2Te_{3.3}Se_{0.2}$ (BTS) segments on polyimide (PI) filaments interconnected by a liquid metal and encapsulated this with a PDMS elastomer. The p-type BST and n-type BTS segments possess high *ZT* values of 1.0 and 1.2 at 360 K, respectively, due to their low thermal conductivity compared with those of bulk Bi_2Te_3-based TE materials. Enhanced toughness and mechanical stability of the TE strings are obtained owing to the synergy of the toughening effect of the PI filaments and the elastic deformation and decreasing the crack opening displacement (COD) of PDMS. Therefore, the crack propagation is limited and the service life of the TET is extended. Afterwards, TE strings and elastic yarns were semi-automatically woven into a TET, utilizing a textile machine, which demonstrated good stretchability (100% elongation), flexibility (minimum bending radius of 2 mm) and washability (>20 washing cycles). The TET showed a high power density of 0.58 W m^{-2} at ΔT of 25 K (predicted power density of 6.06 W m^{-2} at ΔT = 80 K). With the assistance of finite element analysis, the significance of the fabric's structure on the excellent mechanical and TE performance of the TET has been clarified. The TET demonstrated excellent mechanical and TE properties, with an output voltage of $\sim$0.28 V at an ambient temperature ($T_{ambient}$) of $\sim$8 °C. Practically, the TET can continuously power wearable electronics, including an LED array, thermo-hygrometer, body thermometer, pedometer and electronic watch at ΔT = 16 K at $T_{ambient}$ $\sim$ 8 °C, demonstrating high potential for monitoring environmental and human body vital signals and activities. Moreover, for the first time, the reported TET can continuously and stably generate solid-state cooling of 3.1 K in quiescent air ($T_{ambient}$ $\sim$ 26 °C, relative humidity $\sim$60%) because of the high TE properties of the TE strings and the three-dimensional structure of the TET. This adaptive solid-state cooling textile offers an efficient way of personal thermoregulation.

2. Results

2.1 Design and fabrication of bead-like ternary hierarchically coaxial TE strings

The bead-like ternary hierarchically coaxial TE strings (THC-TES) were made with molding and an ultrafast high-temperature sintering (UHS) process[26] (Fig. 1a and Fig. S1, S2, ESI†). PI filaments were firstly placed in the middle of a mold. Subsequently, p-type and n-type Bi_2Te_3-based TE powders were put into the mold alternatingly and cold-pressed at 200 MPa for 1 h. Afterwards, using two pieces of carbon paper as the heat source, the mold was heated for 30 min (4.5 A, $\sim$61 W) and the demolded string was sintered for 10 s (5.5 A, $\sim$91 W) to obtain the binary hierarchically coaxial TE string (BHC-TES). Then, the p-type $Bi_{0.4}Sb_{1.3}Te_3$ (BST) and n-type $Bi_2Te_{3.3}Se_{0.2}$ (BTS) segments in BHC-TES were connected by a liquid metal and encapsulated by PDMS to form the bead-like THC-TES. The 1.2 m-long THC-TES could be bent (bending radius of $\sim$2 mm; bending angle of $\sim$180°) and knotted without damage, showing excellent flexibility and stability (Fig. 1b and Movie 1, ESI†). The field emission scanning electron microscope (FESEM) images (Fig. S3, ESI†)

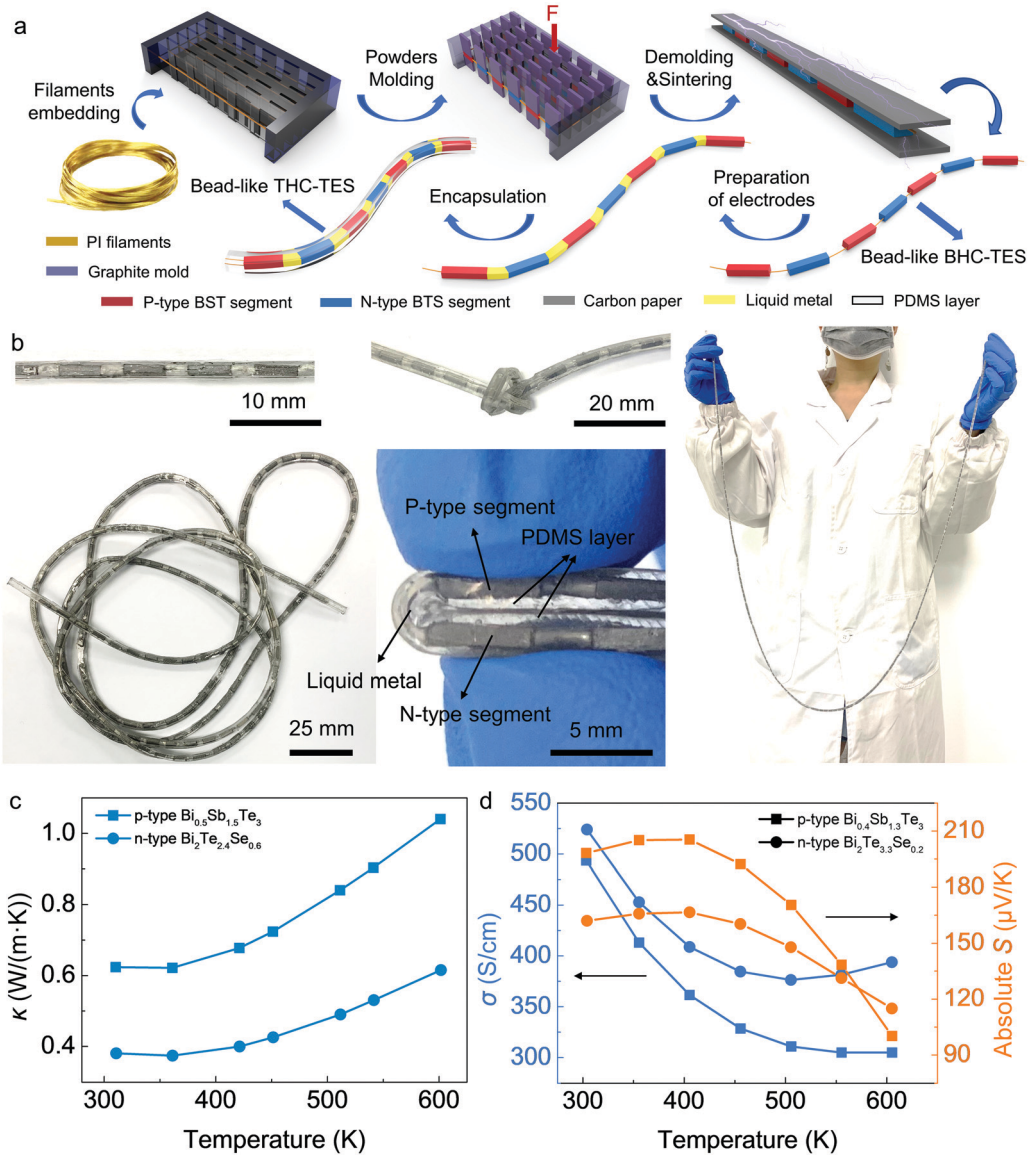

Fig. 1 Production of the bead-like THC-TES. a. The simplified manufacturing process of the TE string. Step 1: PI filaments are embedded in the middle of holes in a graphite mold as a complete sequence. Step 2: p-type and n-type TE powders are put into the mold alternatingly and pressed under a pressure of 200 MPa for 1 h with the help of a tungsten steel frame on the outside of the graphite mold. Step 3: The bead-like string is demolded and sintered through a UHS process (applied current is 5.5 A; applied power is ~91 W) to obtain BHC-TES. Each p-type/n-type segment in BHC-TES is ~5 mm. Step 4: $Ga_{75}In_{25}$ liquid metal is used as the inter-electrode to electrically connect p-type and n-type TE segments. The length of each liquid metal electrode is ~2 mm. Step 5: The string is encased and encapsulated with a PDMS layer to form the bead-like THC-TES. The thickness of the PDMS layer is ~0.5 mm. b. Optical images of ~1.2 m long THC-TES with excellent flexibility. The bead-like THC-TES can be knotted and bent (bending radius is ~2 mm; bending angle is ~180°). c and d. Temperature-dependent TE properties of BST w/-UHS and BTS w/-UHS: total thermal conductivity (c), electrical conductivity and absolute Seebeck coefficient (d).

demonstrate that the TE particles are well fused together in p-type BST and n-type BTS segments after the UHS process (BST w/-UHS and BTS w/-UHS) compared with p-type BST and n-type BTS segments without the UHS process (BST w/o-UHS and BTS w/o-UHS). The material loss during the UHS process is negligible, and the original element compositions of the p-type and n-type powders are maintained (Fig. S3 and Table S1, ESI†). The BST w/-UHS and BTS w/-UHS are crystalline, as proved by the X-ray diffraction (XRD) results (Fig. S4, ESI†).

Afterwards, we measured the temperature-dependent TE properties of BST w/-UHS and BTS w/-UHS (Fig. 1c, d and Fig. S5, ESI†). We found that the total thermal conductivity (κ) of both BST w/-UHS (0.62 W m^{-1} K^{-1} at 303 K) and BTS w/-UHS (0.38 W m^{-1} K^{-1} at 303 K) are significantly reduced, compared to those of p-type and n-type Bi_2Te_3-based bulk materials (1.5–2.5 W m^{-1} K^{-1} at 300 K[27,28]). The electronic thermal conductivity (κ_e) of BST w/-UHS and BTS w/-UHS were calculated to be 0.30 W m^{-1} K^{-1} and 0.28 W m^{-1} K^{-1} at 303 K. The calculated

lattice thermal conductivities (κ_l), by subtracting κ_e from κ, are 0.32 W m^{-1} K^{-1} for BST w/-UHS and 0.10 W m^{-1} K^{-1} for BTS w/-UHS. On the other hand, the electrical conductivity (σ) of BST w/-UHS and BTS w/-UHS are 493 S cm^{-1} and 524 S cm^{-1} at 303 K, respectively, which are smaller than those of zone-melted p-type and n-type Bi_2Te_3-based materials ($\sim$1000 S cm^{-1}).[29]

The low thermal and electrical conductivity can be ascribed to the porous structure of BST w/-UHS and BTS w/-UHS (Fig. S3, ESI†). The measured geometric densities of BST w/-UHS and BTS w/-UHS are 5.0 g cm^{-3} and 5.7 g cm^{-3}, respectively, which are lower than those of bulk p-type and n-type Bi_2Te_3-based TE materials (6.5–7.5 g cm^{-3}). The existence of meso-pores in these samples was proved with Brunner–Emmett–Teller (BET) measurements. Both BST w/-UHS and BTS w/-UHS show large meso-pore volumes in the pore width $<$10 nm (Fig. S6, ESI†). The phonon mean free path in Bi_2Te_3-based TE materials ($<$10 nm[30–35]) matches the pore size distribution, thus likely resulting in significant phonon scattering[36–38] and, thus, κ_l reduction.[39,40] On the other hand, pores can also suppress carrier transport, leading to reduced σ and κ_e.

The Seebeck coefficients (S) of BST w/-UHS and BTS w/-UHS are 198 μV K^{-1} and $-$162 μV K^{-1} at 303 K, respectively, which are comparable to those of zone-melted p-type and n-type Bi_2Te_3-based TE materials (200 μV K^{-1} for $Bi_{0.4}Sb_{1.6}Te_3$[27] and $-$160 μV K^{-1} for $Bi_2Sb_{2.7}Te_{0.3}$[41]). Finally, the ZT values of BST w/-UHS and BTS w/-UHS are 0.96 and 1.12 at 303 K (Fig. S5, ESI†). In addition, with an elevated temperature, high ZT values of 1.0 for BST w/-UHS and 1.2 for BTS w/-UHS at $\sim$360 K are obtained.

2.2 Understanding the mechanical stability of the ternary hierarchically coaxial TE string

As previously mentioned, Bi_2Te_3-based TE materials are usually rigid and brittle, so the toughness and mechanical stability of them is highly important to produce durable TEGs. Here, we investigated the toughness and mechanical stability of THC-TES through experimental characterization and theoretical simulation.

Three-point bending tests with *in situ* resistance measurements were carried out to investigate the mechanical properties of the four samples: TE bulk (TEB), BHC-TES, binary hierarchically coaxial TE bulk (BHC-TEB) and THC-TES (Fig. S7, ESI†). Under bending load conditions, the applied mechanical energy can be absorbed by the deformation, crack propagation and debonding between TE bulk and reinforcement. The typical load-deflection curves of brittle, nonbrittle and elastic fracture are shown in Fig. 2a.[43–45] Similar to the beginning of Line III in Fig. 2a, the load-deflection curve of THC-TES shows ''elastic–plastic'' nonlinear responses at the beginning (Fig. 2b) due to the energy absorption of the PDMS elastomer. As the bending load continues, a sudden load drop appears in the THC-TES and this can be attributed to the quick crack propagation in BTS, resulting in a quick resistance change of $\sim$10% (Fig. 2c). Afterwards, the load redistribution and oscillation show up in THC-TES because of energy absorption in PDMS and load transfer from BTS to the PI filaments. As a result, the resistance of BTS almost remains constant (Fig. 2c). Finally, the debonding between PI filaments and BTS occurs and PI filaments will be pulled out from BTS, leading to a plateau in the load-deflection curve and a further resistance increase of 5.5%.

The interfacial bonding between BTS and sintered PI filaments is predicted using EDS and XPS measurements (Fig. S8, ESI†). On the interface between PI filaments and BTS, we observe oxidative states for the Te element from the XPS spectrum, but EDS mapping for BTS that is far away from sintered PI filaments shows no oxygen element, indicating that covalent bonds should exist between BTS and sintered PI filaments. Therefore, compared with TEB, BHC-TES and BHC-TEB (Note 1, ESI†), the multiple energy absorption form in THC-TES leads to a more stable electrical resistance (Fig. 2c) and good energy absorption of 3.46 mJ (Fig S9, ESI†).

In order to gain further insights into the good mechanical stability of THC-TES, we employed finite element analysis to theoretically investigate the quasi-static crack propagation and stress distribution. Meanwhile, other control samples, including TEB, BHC-TES and BHC-TEB, were also simulated for comparison (Methods, Fig. S10 and Table S2, ESI†). During the whole simulation process, the maximum tensile stress (MTS) criterion was used to determine the crack growth.[42] In Fig. 2d, the crack propagation paths in TEB and BHC-TEB are firmly along the x-axis, indicating the brittle fracture. However, in both BHC-TES and THC-TES, the primary crack propagates along the x-axis first and then shows crack deflection around the PI filament, which demonstrates the typical toughening effect on BTS. Finally, crack coalescence shows up when the crack passes through PI filaments, leading to the complete fracture of BTS. Furthermore, compared with TEB, in which the stress localizes at the crack tip as the crack grows, the stress of BHC-TES localizes at the crack tip first and then the PI filament when the crack propagates at the interface between BTS and the PI filament (Fig. 2e and Movie 2, ESI†). This interesting phenomenon further confirms the toughening effect of the PI filament on BTS. For BHC-TEB, the stress localizes at the crack tip and crack opening (Fig. 2e and Movie S2, ESI†), which demonstrates that the PDMS layer can decrease the crack opening displacement (COD) of BTS. The synergistic effect of the PI filament and PDMS layer result in the toughening effect and decrease of the COD of THC-TES, leading to the most stable mechanical properties, as shown in Fig. 2e and Movie S2 (ESI†). The stress at the crack tip with different crack growth lengths of the aforementioned four samples is shown in Fig. S11 (ESI†).

2.3 Thermoelectric power generation of the TET

Because of the excellent mechanical stability and flexibility of THC-TES, we used a semi-automatic weaving machine to fabricate a 3D multilayer woven TET using the elastic yarns as warp yarns and cotton yarns and THC-TES as weft yarns (Fig. 3a, b, Fig. S12, S13 and Movie S3, ESI†). The TE segments are placed in the thickness direction in the TET, which ensures the direct power generation on the human body. The density of TE

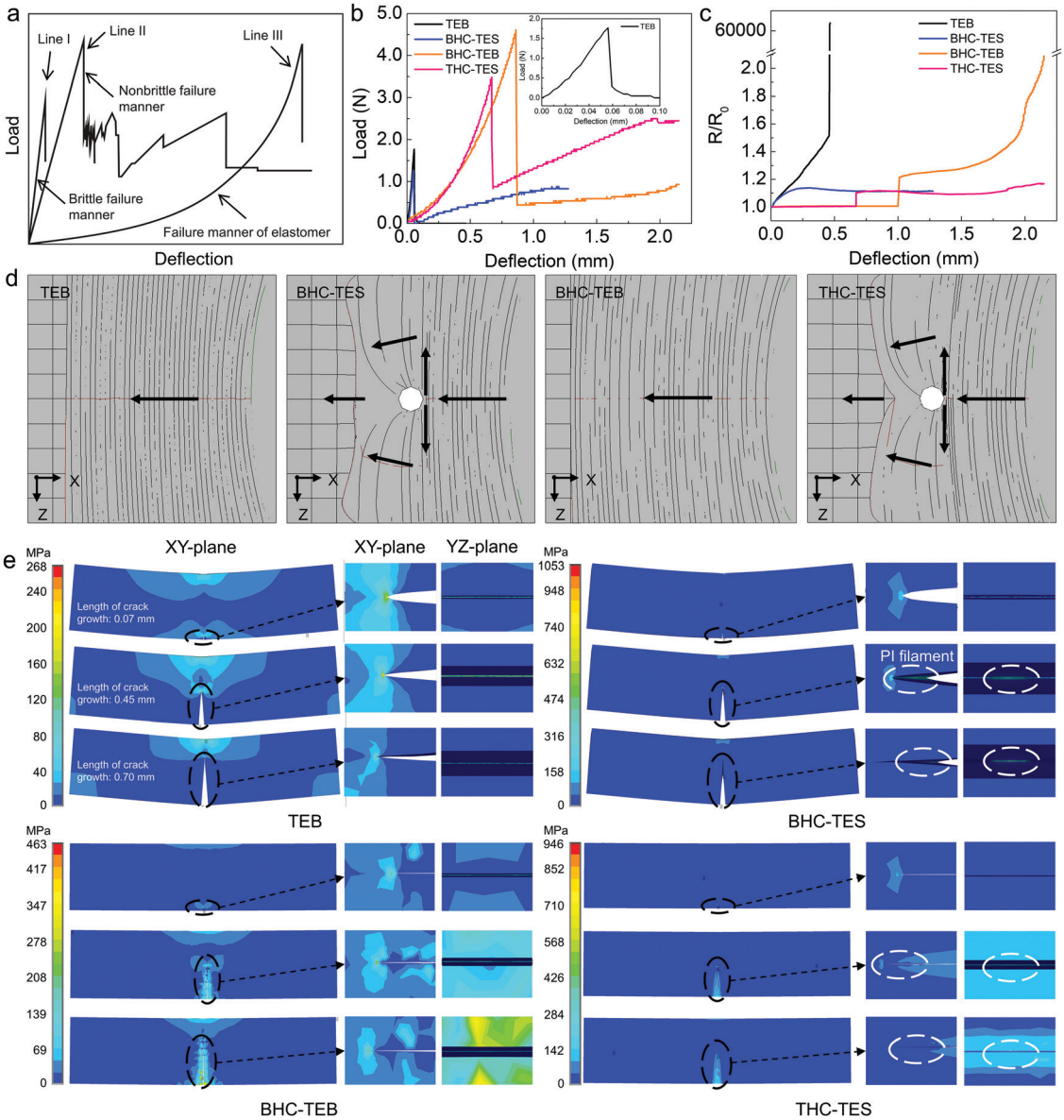

Fig. 2 The mechanical and electrical stability of THC-TES. a. The typical load-deflection curves of brittle, nonbrittle and elastic failure manner.[43–45] b and c. The load-deflection curves (b) and *in situ* resistance change (c) of TEB, BHC-TES, BHC-TEB and THC-TES during three-pointing bending tests. d. The simulated crack propagation path of TEB, BHC-TES, BHC-TEB and THC-TES under three-point bending conditions. The arrows in each diagram show the crack propagation path. The simulated results are achieved by ANSYS and FRANC3D software. e. The stress intensity contours of TEB, BHC-TES, BHC-TEB and THC-TES when the crack growth lengths are 0.07 mm (top), 0.45 mm (middle) and 0.70 mm (bottom). The two figures on the right are the enlarged crack tip region in the figures on the left for each model. Other contours of BHC-TES, BHC-TEB and THC-TES have the same meaning as those of TEB.

segments in TET is ~3–4 pairs cm^{-2}. The TET shows excellent stretchability (100% elongation, Fig. 3b) due to the configuration design of the TET and intrinsic elastic characteristics of the warp yarns. Moreover, it also displays good flexibility with a minimum bending radius of ~2 mm. It can be bent, twisted and even knotted (Fig. 3b). Hence, the TET demonstrates good conformability to a dynamic curved body surface. The output voltage and power density of the as-prepared TET under a small but practical ΔT were measured and under ΔT = 50 K and 80 K were predicted (Fig. 3c, d and Fig. S14, Note S2, Tables S3, S4, ESI†). As shown in Fig. 3c and Fig. S14a (ESI†), the voltage output increases as the applied ΔT enlarges, showing a voltage density up to 177 V m^{-2} at ΔT = 25 K (predicted voltage density of 575 V m^{-2} at ΔT = 80 K). The short circuit current is negatively linearly related to the output voltage, achieving a short circuit current of ~12.5 mA at ΔT = 25 K (predicted short circuit current of ~40.69 mA at ΔT = 80 K). In Fig. 3d, the maximum power density P_{max} of TET reaches up to 0.58 W m^{-2} at ΔT = 25 K when the external resistance R is 30.1 Ω (predicted power density of 6.06 W m^{-2} at ΔT = 80 K). Higher output

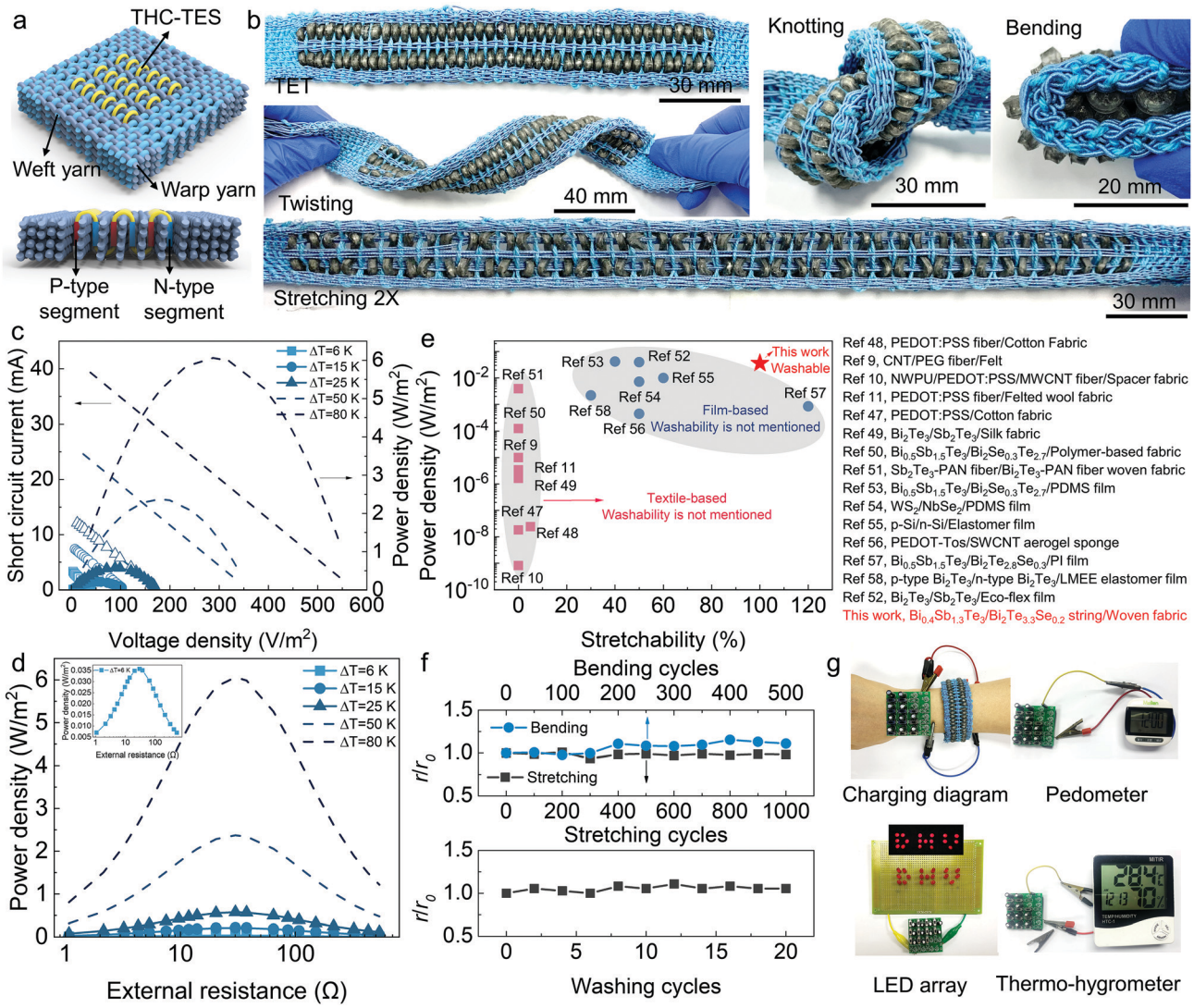

Fig. 3 Structure and thermoelectric power generation of the TET. a. Diagrams of the TET (top: overall view; bottom: side view, demonstrating the alternating vertical arrangement of p-type and n-type segments). b. Optical images illustrating the flexibility (including twisting, knotting and bending) and stretchability of TET. Bending radius of TET is ~2 mm. The TET can be stretched 100%. c. Short circuit current and power density as a function of the voltage density at different ΔT. Note: The data for ΔT = 6 K, 15 K and 25 K were measured and for ΔT = 50 K and 80 K were predicted. d. Output power density of TET as a function of external resistance at different ΔT. Note: The data for ΔT = 6 K, 15 K and 25 K were measured and for ΔT = 50 K and 80 K were predicted. e. The comparison of the power density of the TET in this work with the data reported in the literature, including 3D textile-based and film-based TEGs.[9–11,47–58] Note: the applied ΔT is 6 K. f. The internal resistance change of the TET after stretching, bending and washing. Note: r is the internal resistance of the TET; r_0 is the initial internal resistance of the TET. g. Diagram of charging supercapacitors by putting the TET on the arm of the body and optical images of powering a pedometer, LED array and thermo-hygrometer by the charged supercapacitors.

voltage and power can be further realized by preparing the TET with a larger area or enlarging the applied ΔT.

For TEGs, diminishing the contact resistance between inter-electrodes and TE materials is important for TE power generation. The contact resistivity of the as-prepared TET is calculated to be 380 μΩ cm^2, which is in the range of reported contact resistivities between electrodes and TE materials[46] (Fig. S15, S16 and Table S5, ESI†). We summarize the TE output power density of reported 3D organic-based and inorganic-based flexible TEGs with an applied ΔT of 6 K. With excellent stretchability and flexibility, the output power density of the TET in this work outperforms all of the textile based ones[9–11,47–51] and is comparable to that of traditional non-textile based ISC-based flexible TEGs[52,53] (Fig. 3e), showing great promise for portable and wearable power generation systems. Furthermore, the internal resistance of the TET is not significantly affected by cyclic 100% stretching (>1000 cycles) and bending over 500 times, even though THC-TES in the TET will bear cyclic mechanical bending (Fig. 3f, Note S3 and Fig. S17, ESI†). Thanks to the PDMS encapsulation layer and the mechanically stable structure of THC-TES, the TET can be washed by a washing machine as a common fabric (>20 washing cycles) with very stable TE properties (Fig. 3g and Movie S4, ESI†).

Similar to traditional TEGs, the thermal and electrical transport in TETs are of key importance for understanding and improving their TE performance. Based on the composition of the TET, we drew the thermal and electrical circuits of the TET, as shown in Fig. 4a and b. When the TET operates in the power generation mode under practical conditions, the heat flux Q flows through the surface of the heat source (human skin) to the top side of the TET, and then into the inner structure of the TET (including the PDMS layer, TE segments, PI filaments and fabric) to the bottom side exposed to ambient conditions. Each component in the TET is supposed to be thermally connected in parallel. Using the data in Fig. 1c and d, we constructed a TET model to understand the thermal and electrical transport in TET with the assistance of finite element analysis (Fig. 18a and Table S6, ESI†). The dimensions, thermal and electrical properties of each component in the TET model are the same as those of the as-prepared TET.

As shown in Fig. 4c–g, when the TET is attached to a heat source of 32 °C at an ambient temperature of ~8 °C, the absorbed heat flows in-parallel through each element in the TET and dissipates the remaining heat through its cold side to the ambient environment (Fig. 4a). Since the heat conduction is dominant over the Peltier and Joule heating under the maximum power output conditions, the established ΔT is positively proportional to the total thermal resistance of the TE device, suggesting that increasing the thermal resistance can improve its TE performance. At a given thermal resistance of TE segments, the equivalent thermal resistances of each non-TE component in the TET, including the encapsulation layer (PDMS), inter-electrode (liquid metal), PI filaments and textile

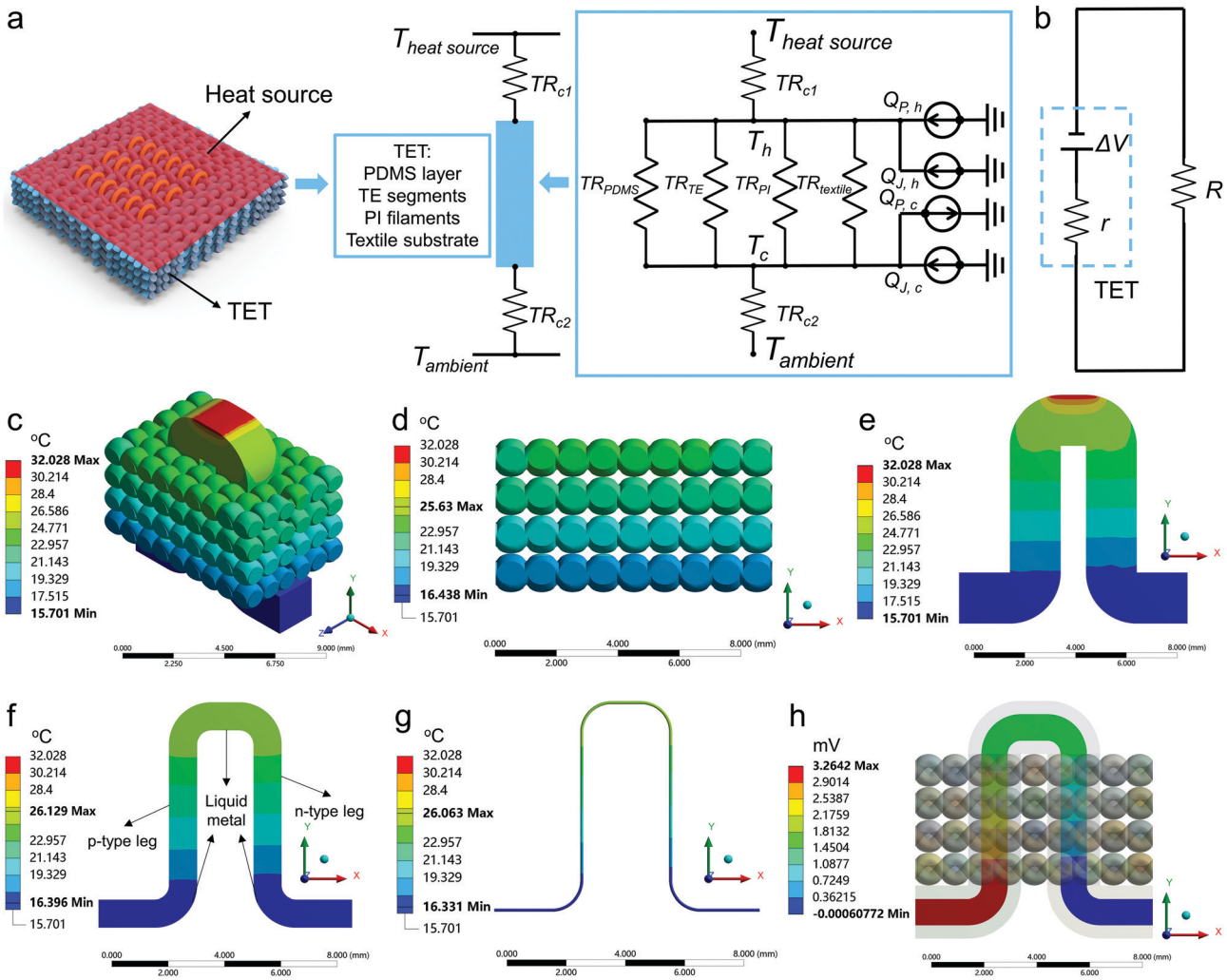

Fig. 4 The thermal and electrical transport in the TET. a. The thermal diagram during thermal transport in the TET. Note: TR represents the thermal resistance (TR_{c1} and TR_{c2} are the contact thermal resistances at the hot side and cold side, respectively, and TR_{PDMS}, TR_{TE}, TR_{PI} and $TR_{textile}$ are the thermal resistances of the PDMS layer, TE segments, PI filaments and textile substrate, respectively). Q represents the generated input heat ($Q_{P,h}$ and $Q_{P,c}$ are the input heats generated by the Peltier effect at the hot side and cold side, respectively; $Q_{J,h}$ and $Q_{J,c}$ are the input heats generated by Joule heating at the hot side and cold side, respectively). b. The electrical diagram of the TET during electrical transport in the TET. Note: r is the internal resistance of the TET. R is the external resistance. c. The temperature distribution of the TET resulting from finite element analysis. d–g. The temperature distribution of the textile substrate (d), PDMS layer (e), p-type leg, n-type leg and inner-electrode (f) and PI filament (g). h. The electrical potential distribution of the TET.

fabric, should be as high as possible. In this work, the self-built ΔT is ~16.3 K, resulting in the simulated output voltage of ~3.26 mV for one pair of p–n segments (Fig. 4h). Furthermore, we applied a series of ΔT on the TET in the thickness direction to verify the thermal transport and output performance of the TET. The output voltage increases linearly with the elevated ΔT and is slightly higher than the measured data at each ΔT (Fig. S19a, Note S4 and Tables S7, S8, ESI†).

We further wore the TET on the arm using the temperature gradient established between the body surface and the surroundings in cool weather. The TET generated a stable voltage of ~0.2 V when the ambient temperature was ~8 °C (ΔT ~ 16 K, Fig. S20, ESI†), which is 73.7% of the simulated output voltage due to the existence of contact thermal and electrical resistance in the as-prepared TET. Afterwards, ten pieces of supercapacitor (POWERSTOR Series B, 2.5 V 0.22 F) connected in parallel were charged to ~0.2 V and then switched to the in-series mode (output voltage ~1.7 V). The supercapacitors successfully powered a series of wearable electronics, such as a LED array, thermo-hygrometer, pedometer, body thermometer and electronic watch for monitoring the environment, human body activities and vital signals (Fig. 3g, Fig. S21 and Movie S5, ESI†). The supercapacitors were re-charged in the in-parallel mode when the voltage of the supercapacitor connected electronics was less than 1.2 V. As shown in Fig. S21e (ESI†), the charging time (~3.6 min for the initial charging and ~1.2 min for recharging) is much shorter than the discharging time (30.6 min), indicating that the TET can continuously and stably generate enough electricity to power electronics. The output voltage of TET on human body is not affected by human motion, such as elbow bending, swinging and wrist bending. Interestingly, the TE performance of the TET is enhanced by body motion due to enhanced air convection (Fig. S22, ESI†).

2.4 Personal thermoregulation by the TET

Thermoregulating the microclimate around the human body plays a vital role in reducing energy consumption compared to conventional air conditioners, which has never been realized in textile based TEGs. Here, for the first time, we obtained a solid-state cooling fabric which can stably reduce the temperature of human skin. In this section, with the assistance of finite element analysis (Fig. S18b and Table S6, ESI†) and experiment characterizations, we investigated the solid-state cooling effect of the TET by applying a direct current (0–160 mA). As shown in Fig. 5a–c, the TET shows an obvious cooling effect (temperature decrease for TET is ~3.1 K) due to the high Seebeck coefficient, electrical conductivity and low thermal conductivity of the TE materials (Fig. 1c, d and Fig. S5, ESI†), as well as the optimal thermal properties of the non-TE components. Afterwards, we verified the cooling effect by placing the TET on an insulated bracket and inputting a series of currents. The temperature at the cold side was monitored and recorded by a thermal infrared camera (Fotric 226). In quiescent air ($T_{ambient}$ ~ 26 °C/37 °C, relative humidity ~60%), maximum temperature reductions of 3.1 K and 2.3 K are obtained under an applied current of 140 mA when the initial temperatures of the TET are 26.3 °C and 37 °C, respectively (Fig. 5d, e and Movie S6, ESI†). However, when the applied DC current further increases, the temperature reduction will be suppressed due to Joule heating. At a given applied DC current, the temperature of the cold surface begins decreasing instantaneously and reaches a plateau within a few minutes. The temperature at the cold side of the TET can be maintained stably over 30 min (Fig. 5f). The simulating temperature drop of the cold side is higher than the measured one because the electrical contact resistance between the electrodes and TE materials is ignored in the simulation (Fig. S19b, ESI†).

Theoretically, when the TET operates in the Peltier cooling mode (Fig. 4a), the current I flows through the TE strings. As a result, the TET absorbs heat at one joint (T_1) and releases heat at another joint (T_2, $T_2 > T_1$), thus establishing a temperature difference $\Delta T = T_2 - T_1$ in the thickness direction. According to the Peltier effect, the pumping heat from the cold side to the hot side per unit time $Q_P = \pi_{TET} I$ (π_{TET} is the Peltier coefficient), which can also be written as $Q_P = S_{TET} T_1 I$. In addition, heat conduction from the hot side to the cold side will also occur when there is a temperature difference. Assuming that the total thermal conductivity of the TET is κ', the specific heat flow is $\kappa'(T_2 - T_1)$. Moreover, the Joule heating in the TET is generated from TE segments (16.9 Ω) and contact resistance between TE segments and inter-electrodes (13.1 Ω) and inter-electrodes (0.1 Ω). Therefore, the Joule heating $I^2 r$ will transport equally to the hot side and the cold side of the TET, that is, the heat flowing into the cold side/hot side due to Joule heat per unit time is $Q_{J,c} = Q_{J,h} = \frac{1}{2} I^2 r$, where r is the total internal resistance (30.1 Ω). In the steady-state, all the heat inputs and outputs are balanced at each joint of the thermal circuit. Therefore, the cooling capacity of the TET can be calculated by the equation:[59] $Q_c = S_{TET} T_1 I - \frac{1}{2} I^2 r - k' \Delta T$, where S_{TET} is the Seebeck coefficient of the TET, T_1 is the temperature of the cold surface, I is the input current, r is the internal resistance of the TET, Q_c is the cooling capacity and k' is the thermal conductivity of the TET. Hence, the higher Seebeck coefficient of TE materials, and the lower internal resistance and the thermal conductivity of the TE devices will contribute to the higher cooling capacity. In addition, there exists an optimal input current to achieve maximum ΔT due to the trade-off between Peltier cooling and Joule heating.

Subsequently, we calculated the cooling capacity, maximum cooling capacity, maximum attainable temperature difference and *COP* of the TET (Note S5–S8, Tables S9–S13 and Fig. S23, ESI†). Since the S_{TET} positively depends on the number of TE couples, a larger cooling capacity can be obtained through a larger size of the TET. Furthermore, the maximum specific cooling capacity of the TET at ΔT = 0.5 K is as high as 162.4 W m^{-2}. The maximum cooling capacity, maximum attainable temperature difference and *COP* of TET are calculated to be 0.374 W (ΔT = 0.5 K), 5.3 K and 4.85, respectively.

Finally, we demonstrated the personal thermoregulation of the human body under indoor conditions ($T_{ambient}$ ~ 26 °C, relative humidity ~60%). A remaining temperature drop of 1.9 K on the

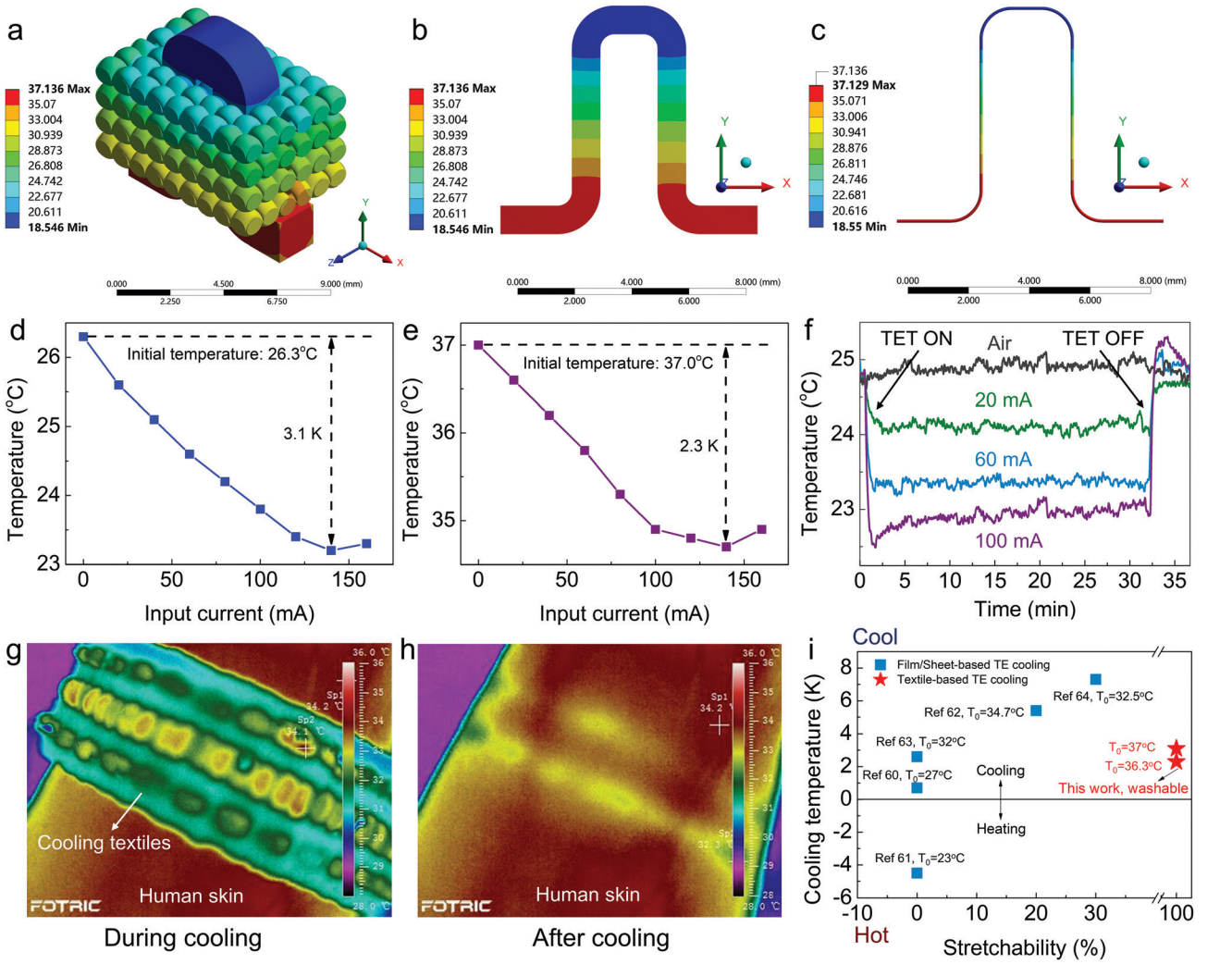

Fig. 5 The thermoregulation of the TET. a–c. The temperature distribution of the simulated TET (a), p-type leg, n-type leg and inner-electrode (b) and PI filament (c). Note: The input current is 140 mA. The temperature of ambient air is 26.3 °C. d and e. The temperature change of the TET with different applied currents when the initial temperature is 26.3 °C (d) and 37 °C (e). f. Time-dependent cooling effect of the TET. g and h. The demonstration of thermal regulation on the human body. The skin temperature is 34.2 °C before cooling (g). After cooling, the skin temperature is reduced to 32.3 °C (h). i. The comparison of the cooling effect (temperature drop) of the TET in this work with the data reported in the literature.[60–64] Note: The positive cooling temperature means temperature decrease; the negative cooling temperature means temperature increase. T_0 represents the initial temperature of cold side.

human arm was continuously detected after the quick removal of the TET, indicating a realistic application potential in personal thermoregulation using the TET (Fig. 5g, h, Movie S7, ESI†). In terms of excellent flexibility and stretchability, our TET, with an obvious temperature reduction, outperforms the majority of reported flexible TE coolers[60–64] (Fig. 5i).

3. Discussion

In conclusion, we designed and manufactured a new type of bead-like ternary hierarchically coaxial TE string (THC-TES) configured with alternating p-type BST and n-type BTS segments interconnected by liquid metal on PI filaments and further encapsulated with a PDMS elastomer. The THC-TES showed enhanced toughness and mechanical stability under three-point bending load conditions compared with those of TE bulk. The THC-TES was semi-automatically woven into a flexible and stretchable TET using a textile machine, which showed a good washability (>20 washing cycles) and high power density of 0.58 W m^{-2} at ΔT = 25 K (predicted power density of 6.06 W m^{-2} at ΔT = 80 K). Furthermore, various wearable electronics can be powered by wearing the TET on a human arm ($T_{ambient}$ ~ 8 °C). Moreover, the TET in quiescent air ($T_{ambient}$ ~ 26 °C, relative humidity ~60%) can continuously and stably generate solid-state cooling of 3.1 K in the thickness direction and 1.9 K cooling effect on the arm of the body.

4. Experimental

4.1 Materials

PI filaments (Jiangsu Shino New Materials Technology Co., Ltd) were cleaned with ethanol, acetone and DI water by an ultrasonic machine before using. P-type BST and n-type BTS TE

powders (Wuhan Xinrong New Materials Co., Ltd) were used as received. The ratio of PDMS precursor and curing agent (Dow Corning, Sylgard184) was 10 : 1. $Ga_{75}In_{25}$ liquid metal (Zhongxi Alloy Co., Ltd) was used as received. Elastic yarns (spandex–polyester core-spun yarn, diameter: 0.5 mm) and lace yarns (MaiXianXian, 6S/3, 100% cotton) were used as received.

4.2 Preparation of bead-like ternary hierarchically coaxial TE strings

Cleaned PI filaments were placed in the middle of each graphite mold in a complete sequence (the diameter of PI filaments was ~0.1 mm). The tungsten steel load-bearing sheets (5 × 4.5 mm^2) were put into the holes (1 × 5 × 10 mm^2) between each graphite mold on one side. The p-type and n-type TE powders were put into the holes between each graphite mold on the other side alternatingly. And then, the holes containing TE powders were blocked with tungsten steel load-bearing sheets (5 × 5.5 mm^2). Afterwards, the whole graphite mold was placed in a tungsten steel frame and a pressure of 200 MPa was applied for 1 h through a universal testing machine (Shenzhen Labsans Testing Machine Co., Ltd) to mold the TE powders. The graphite mold was demolded from the tungsten steel frame and heated through two pieces of carbon paper (Toray, TGP-H-060, 62 mm in length, 12 mm in width and 0.19 mm in thickness) under a current of 4.5 A for 30 min under Ar atmosphere (supply power was ~61 W). The BHC-TES was demolded from the graphite mold when the mold cooled down to room temperature. Subsequently, the BHC-TES was sintered through the two pieces of carbon paper under a current of 5.5 A for 10 s under Ar atmosphere (the input power was ~91 W). The liquid metal was brushed onto the surface of the TE segment with a cotton swab to pre-wet the connecting surface. And then, the liquid metal was injected and coated on the PI filaments to connect the p-type and n-type TE segments. A mixture of PDMS precursor and curing agent (ratio of precursor and curing agent was 10 : 1) was injected into a 3D printed mold (2 mm in width and 2 mm in depth) to 0.5 mm-thick and pre-cured at 55 °C for 30 min. Subsequently, the BHC-TES coated with liquid metal was placed on the pre-cured PDMS layer. The mixture of PDMS precursor and curing agent was injected into the mold again until it fully filled the mold. Finally, the bead-like THC-TES was cured and demolded.

4.3 Morphology characterization

The microscopic morphology characterization and EDS elemental analysis were performed by a FESEM (Hitachi, SU8010 series) using an accelerating voltage of 5.0 kV (morphology) and 10.0 kV (EDS) and a work distance of ~8 mm (morphology) and ~15 mm (EDS).

4.4 Temperature dependent thermoelectric property measurements

The samples used in the temperature dependent thermoelectric property measurements were manufactured with the same method and parameters shown in Fig. S1 (ESI†). The size of the sample for the electrical conductivity (σ) and Seebeck coefficient (S) measurements was 2 × 2 × 10 mm^3 and for the thermal conductivity (κ) measurement it was 10 mm in diameter and 1.5 mm in thickness. The σ and S were measured simultaneously using a commercial system (ULVAC ZEM-3). The thermal diffusivity (D) was measured using the laser flash method (Netzsch, LFA-457). The specific heat (C_p) (0.19 J g^{-1} K^{-1} for p-type BST w/-UHS and 0.16 J g^{-1} K^{-1} for n-type BTS w/-UHS) was determined by differential scanning calorimetry using a Netzsch DSC 404F3. The density (d) was measured by the geometric method. The total thermal conductivity (κ) was calculated according to the relationship $\kappa = dC_pD$. The electronic thermal conductivity (κ_e) was calculated according to the equation: $\kappa_e = L\sigma T$, where L_0 is the Lorenz number, σ is the electrical conductivity and T is the absolute temperature.

4.5 FEA simulation of the TE materials

In order to simplify the simulation process, four n-type BTS segment models (Fig. S10, ESI†) which featured TEB (1 × 1 × 5 mm^3), BHC-TES (size of BTS was 1 × 1 × 5 mm^3, diameter of the PI filament was 0.1 mm), BHC-TEB (size of BTS was 1 × 1 × 5 mm^3, thickness of the PDMS layer was 0.5 mm) and THC-TES (size of BTS was 1 × 1 × 5 mm^3, thickness of the PDMS layer was 0.5 mm, diameter of the PI filament was 0.1 mm) were constructed and meshed based on ANSYS (Version 19.2) software. Under conditions of three-point bending, a fixed pressure of 5 N was applied onto the top middle surface of each sample (0.1 × 1 mm^2) while the bottom right and left edges were fixed. The models were input and post-processed in FRANC3D (Version 7.5.6) software, and all the crack growth simulation parameters were set in FRANC3D and solved by ANSYS.

4.6 The fabrication process of the TET

The TET was woven by a semi-automatic weaving machine (Jiangyin Tongyuan Textile Machinery Co., Ltd, SGA598). The reed count used in the weaving process was 22#. The TET was a 3D woven fabric with four layers. The diagrams of the draft plan, denting plan and lifting plan are shown in Fig. S13 (ESI†).

4.7 Washing process of the TET

The TET was washed by a household drum washing machine (SIEMENS, IQ300). The washing time was set to be 30 min, including washing and drying processes. The temperature of the water was ~20 °C.

4.8 Demonstration of practical applications of the TET for wearable electronics

The ambient temperature of ~8 °C was achieved by a refrigerator. Ten pieces of commercial supercapacitor (2.5 V, 0.22 F) in the in-parallel mode were charged by the TET through wearing it on the arm. A circular aluminum heat sink was attached on the surface of the TET exposed to the cold surroundings. Afterwards, the ten pieces of charged supercapacitors were switched to the in-series mode by a switching circuit and then powered the LED array, thermo-hygrometer, pedometer, body thermometer and electronic watch.

Data availability

The data supporting our findings in this work are available from the corresponding author K. Z. upon reasonable request.

Author contributions

K. Z. and Y. Z. conceived of the idea and designed the experiments. K. Z. and G. L. supervised the project. Y. Z. and X. H. designed and optimized the molding parameters of TES. Q. L. helped in the cold-pressed experiment during the TES manufacturing process. Y. Z. prepared all TES and TET samples. Y. Z. performed the modeling and finite element simulation and data analysis. Y. Z., Y. J. and X. C. designed the structure of the TET. Y. Z. and J. Y. conducted the thermoelectric property measurements of the TET. Y. Z. measured the cooling effect of the TET. T. Z., H. T. Z., H. Z. Z. and G. J. S. provided valuable suggestions during the whole project. Y. Z. conducted device demonstrations, drew figures and made supporting movies. Y. Z, K. Z. and G. L. prepared the initial manuscript. All authors discussed the results and contributed to reviewing the manuscript.

Conflicts of interest

There are no conflicts to declare.

Acknowledgements

K. Z. is grateful for the funding support from the National Natural Science Foundation of China (grant no. 51973034) and the Fundamental Research Fund for the Central Universities (grant no. 2232020G-01 and 19D110106). K. Z. also acknowledges the support from the Research Base of Electronic Textile Materials and Products, China Textile Engineering Society. G. Li, H. Zhu, and H. Zhao acknowledge the funding support of the National Key Research and Development Program of China (grant no. 2018YFA0702100) and the National Natural Science Foundation of China (grant no. 52172259 and 52172262). T. Z. thanks the financial support from the National Natural Science Foundation of China (grant no. 52172249), and the Funding of the Innovation Academy for Light-duty Gas Turbine, Chinese Academy of Sciences (grant no. CXYJJ21-ZD-02). We acknowledge the help of Dr Pengfei Qiu from the Shanghai Institute of Ceramics, Chinese Academy of Sciences with the thermoelectric property measurements of p-type BST w/-UHS and n-type BTS w/-UHS.

References

1 S. Ahn, Y. Cho, S. Park, J. Kim, J. Sun, D. Ahn, M. Lee, D. Kim, T. Kim, H. Shin and J.-J. Park, *Nano Energy*, 2020, **74**, 104932.
2 L. Ma, R. Wu, S. Liu, A. Patil, H. Gong, J. Yi, F. Sheng, Y. Zhang, J. Wang, J. Wang, W. Guo and Z. L. Wang, *Adv. Mater.*, 2020, **32**, 2003897.
3 F. Wen, Z. Sun, T. He, Q. Shi, M. Zhu, Z. Zhang, L. Li, T. Zhang and C. Lee, *Adv. Sci.*, 2020, **7**, 2000261.
4 Y. Zheng, Q. Zhang, W. Jin, Y. Jing, X. Chen, X. Han, Q. Bao, Y. Liu, X. Wang, S. Wang, Y. Qiu, C.-A. Di and K. Zhang, *J. Mater. Chem. A*, 2020, **8**, 2984–2994.
5 H. M. Elmoughni, A. K. Menon, R. M. W. Wolfe and S. K. Yee, *Adv. Mater. Technol.*, 2019, **4**, 1800708.
6 G. J. Snyder and E. S. Toberer, *Nat. Mater.*, 2008, **7**, 105–114.
7 D. Zhao and G. Tan, *Appl. Therm. Eng.*, 2014, **66**, 15–24.
8 Y. Peng, J. Chen, A. Y. Song, P. B. Catrysse, P.-C. Hsu, L. Cai, B. Liu, Y. Zhu, G. Zhou, D. S. Wu, H. R. Lee, S. Fan and Y. Cui, *Nat. Sustain.*, 2018, **1**, 105–112.
9 M. Ito, T. Koizumi, H. Kojima, T. Saito and M. Nakamura, *J. Mater. Chem. A*, 2017, **5**, 12068–12072.
10 Q. Wu and J. Hu, *Smart Mater. Struct.*, 2017, **26**, 045037.
11 A. Lund, Y. Tian, S. Darabi and C. Müller, *J. Power Sources*, 2020, **480**, 228836.
12 B. Poudel, Q. Hao, Y. Ma, Y. C. Lan, A. Minnich, B. Yu, X. A. Yan, D. Z. Wang, A. Muto, D. Vashaee, X. Y. Chen, J. M. Liu, M. S. Dresselhaus, G. Chen and Z. F. Ren, *Science*, 2008, **320**, 634–638.
13 J. Mao, G. Chen and Z. F. Ren, *Nat. Mater.*, 2021, **20**, 454–461.
14 T. Ghosh, S. Roychowdhury, M. Dutta and K. Biswas, *ACS Energy Lett.*, 2021, **6**, 2825–2837.
15 S. Roychowdhury, T. Ghosh, R. Arora, M. Samanta, L. Xie, N. K. Singh, A. Soni, J. He, U. V. Waghmare and K. Biswas, *Science*, 2021, **371**, 722–727.
16 M. Dutta, K. Pal, M. Etter, U. V. Waghmare and K. Biswas, *J. Am. Chem. Soc.*, 2021, **143**, 16839–16848.
17 Y. Wang, M. Hong, W.-D. Liu, X.-L. Shi, S.-D. Xu, Q. Sun, H. Gao, S. Lu, J. Zou and Z.-G. Chen, *Chem. Eng. J.*, 2020, **397**, 125360.
18 H. Chen, T.-R. Wei, K. Zhao, P. Qiu, L. Chen, J. He and X. Shi, *InfoMat*, 2021, **3**, 22–35.
19 S. Yang, Z. Gao, P. Qiu, J. Liang, T.-R. Wei, T. Deng, J. Xiao, X. Shi and L. Chen, *Adv. Mater.*, 2021, **33**, 2007681.
20 J. Peng and G. J. Snyder, *Science*, 2019, **366**, 690.
21 T. Zhang, K. Li, J. Zhang, M. Chen, Z. Wang, S. Ma, N. Zhang and L. Wei, *Nano Energy*, 2017, **41**, 35–42.
22 Z. Cao, M. J. Tudor, R. N. Torah and S. P. Beeby, *IEEE Trans. Electron Devices*, 2016, **63**, 4024–4030.
23 S. J. Kim, J. H. We and B. J. Cho, *Energy Environ. Sci.*, 2014, **7**, 1959.
24 P. Wang, K. Wang, B. Wang, C. Zhang and D. J. E. F. M. Fang, *Eng. Fract. Mech.*, 2020, **235**, 107186.
25 G. Li, Q. An, B. Duan, L. Borgsmiller, M. Al Malki, M. Agne, U. Aydemir, P. Zhai, Q. Zhang, S. I. J. M. S. Morozov and E. R. Reports, *Mater. Sci. Eng., R*, 2021, **144**, 100607.
26 C. Wang, W. Ping, Q. Bai, H. Cui, R. Hensleigh, R. Wang, A. H. Brozena, Z. Xu, J. Dai, Y. Pei, C. Zheng, G. Pastel, J. Gao, X. Wang, H. Wang, J.-C. Zhao, B. Yang, X. Zheng, J. Luo, Y. Mo, B. Dunn and L. Hu, *Science*, 2020, **368**, 521–526.
27 J. Jiang, L. Chen, S. Bai, Q. Yao and Q. Wang, *J. Cryst. Growth*, 2005, **277**, 258–263.

28 J. Jiang, L. Chen, Q. Yao, S. Bai and Q. Wang, *Mater. Chem. Phys.*, 2005, **92**, 39–42.
29 K. Kato, Y. Hatasako, M. Uchino, Y. Nakata, Y. Suzuki, T. Hayakawa, C. Adachi and K. Miyazaki, *Adv. Mater. Interfaces*, 2014, **1**, 1300015.
30 A. Mavrokefalos, A. L. Moore, M. T. Pettes, L. Shi, W. Wang and X. Li, *J. Appl. Phys.*, 2009, **105**, 104318.
31 I.-H. Kim, *Mater. Lett.*, 2000, **44**, 75–79.
32 S. Shen, W. Zhu, Y. Deng, H. Zhao, Y. Peng and C. Wang, *Appl. Surf. Sci.*, 2017, **414**, 197–204.
33 B. A. Assaf, T. Cardinal, P. Wei, F. Katmis, J. S. Moodera and D. Heiman, *Appl. Phys. Lett.*, 2013, **102**, 012102.
34 L. Bulat, V. Osvenskii, Y. N. Parkhomenko, D. Pshenay-Severin and A. J. J. O. E. M. Sorokin, *J. Electron. Mater.*, 2016, **45**, 1648–1653.
35 O. Hellman and D. A. Broido, *Phys. Rev. B: Condens. Matter Mater. Phys.*, 2014, **90**, 134309.
36 J. Jin, M. P. Manoharan, Q. Wang and M. A. Haque, *Appl. Phys. Lett.*, 2009, **95**, 033113.
37 I. Sumirat, Y. Ando and S. Shimamura, *J. Porous Mater.*, 2006, **13**, 439–443.
38 D. G. Cahill, W. K. Ford, K. E. Goodson, G. D. Mahan, A. Majumdar, H. J. Maris, R. Merlin and S. R. Phillpot, *J. Appl. Phys.*, 2003, **93**, 793–818.
39 F. Kim, B. Kwon, Y. Eom, J. E. Lee, S. Park, S. Jo, S. H. Park, B.-S. Kim, H. J. Im, M. H. Lee, T. S. Min, K. T. Kim, H. G. Chae, W. P. King and J. S. Son, *Nat. Energy*, 2018, **3**, 301–309.
40 H. Lee, D. Vashaee, D. Z. Wang, M. S. Dresselhaus, Z. F. Ren and G. Chen, *J. Appl. Phys.*, 2010, **107**, 094308.
41 J. Jiang, L. Chen, S. Bai, Q. Yao and Q. Wang, *Mater. Sci. Eng., B*, 2005, **117**, 334–338.
42 D. Mangardich, F. Abrari and Z. Fawaz, *Eng. Fract. Mech.*, 2019, **214**, 474–486.
43 C.-a. Wang, Y. Huang, Q. Zan, L. Zou and S. Cai, *J. Am. Ceram. Soc.*, 2002, **85**, 2457–2461.
44 J. B. Wachtman, W. R. Cannon and M. J. Matthewson, *Mechanical properties of ceramics*, John Wiley & Sons, Hoboken, 2009.
45 J. Gong, *Fracture mechanics of ceramics*, Tsinghua Univ. Press, Beijing, 2001.
46 P. Ziolkowski, P. Poinas, J. Leszczynski, G. Karpinski and E. Müller, *J. Electron. Mater.*, 2010, **39**, 1934–1943.
47 Y. Du, K. Cai, S. Chen, H. Wang, S. Z. Shen, R. Donelson and T. Lin, *Sci. Rep.*, 2015, **5**, 6411.
48 Y. Kim, A. Lund, H. Noh, A. I. Hofmann, M. Craighero, S. Darabi, S. Zokaei, J. I. Park, M.-H. Yoon and C. Müller, *Macromol. Mater. Eng.*, 2020, **305**, 1900749.
49 Z. Lu, H. Zhang, C. Mao and C. M. Li, *Appl. Energy*, 2016, **164**, 57–63.
50 M.-K. Kim, M.-S. Kim, S. Lee, C. Kim and Y.-J. Kim, *Smart Mater. Struct.*, 2014, **23**, 105002.
51 J. A. Lee, A. E. Aliev, J. S. Bykova, M. J. de Andrade, D. Kim, H. J. Sim, X. Lepro, A. A. Zakhidov, J. B. Lee, G. M. Spinks, S. Roth, S. J. Kim and R. H. Baughman, *Adv. Mater.*, 2016, **28**, 5038–5044.
52 Y. Yang, H. Hu, Z. Chen, Z. Wang, L. Jiang, G. Lu, X. Li, R. Chen, J. Jin, H. Kang, H. Chen, S. Lin, S. Xiao, H. Zhao, R. Xiong, J. Shi, Q. Zhou, S. Xu and Y. Chen, *Nano Lett.*, 2020, **20**, 4445–4453.
53 V. Padmanabhan Ramesh, Y. Sargolzaeiaval, T. Neumann, V. Misra, D. Vashaee, M. D. Dickey and M. C. Ozturk, *npj Flex. Electron.*, 2021, **5**, 5.
54 J. Y. Oh, J. H. Lee, S. W. Han, S. S. Chae, E. J. Bae, Y. H. Kang, W. J. Choi, S. Y. Cho, J.-O. Lee, H. K. Baik and T. I. Lee, *Energy Environ. Sci.*, 2016, **9**, 1696–1705.
55 K. Nan, S. D. Kang, K. Li, K. J. Yu, F. Zhu, J. Wang, A. C. Dunn, C. Zhou, Z. Xie, M. T. Agne, H. Wang, H. Luan, Y. Zhang, Y. Huang, G. J. Snyder and J. A. Rogers, *Sci. Adv.*, 2018, **4**, eaau5849.
56 X. Wang, L. Liang, H. Lv, Y. Zhang and G. Chen, *Nano Energy*, 2021, **90**, 106577.
57 W. Ren, Y. Sun, D. Zhao, A. Aili, S. Zhang, C. Shi, J. Zhang, H. Geng, J. Zhang, L. Zhang, J. Xiao and R. Yang, *Sci. Adv.*, 2021, **7**, eabe0586.
58 M. Zadan, M. H. Malakooti and C. Majidi, *ACS Appl. Mater. Interfaces*, 2020, **12**, 17921–17928.
59 R. Chein and G. Huang, *Appl. Therm. Eng.*, 2004, **24**, 2207–2217.
60 W. Hou, X. Nie, W. Zhao, H. Zhou, X. Mu, W. Zhu and Q. Zhang, *Nano Energy*, 2018, **50**, 766–776.
61 H. Wu, X. Liu, P. Wei, H.-Y. Zhou, X. Mu, D.-Q. He, W.-T. Zhu, X.-L. Nie, W.-Y. Zhao and Q.-J. Zhang, *J. Electron. Mater.*, 2017, **46**, 2950–2957.
62 D. Lee, H. Park, G. Park, J. Kim, H. Kim, H. Cho, S. Han and W. Kim, *Energy*, 2019, **188**, 116019.
63 L. Lou, D. Shou, H. Park, D. Zhao, Y. S. Wu, X. Hui, R. Yang, E. C. Kan and J. Fan, *Energy Build.*, 2020, **226**, 110374.
64 S. Hong, Y. Gu, J. K. Seo, J. Wang, P. Liu, Y. S. Meng, S. Xu and R. Chen, *Sci. Adv.*, 2019, **5**, eaaw0536.